# Fluorescence imaging for whole slide scanning using LED-based color sequential illumination

Van Der Graaff, Leon; Boyaval, Fanny; Van Vliet, Lucas J.; Stallinga, Sjoerd

**DOI**
10.1117/12.2306776

**Publication date**
2018

**Document Version**
Final published version

**Published in**
Optics, Photonics, and Digital Technologies for Imaging Applications V

PROCEEDINGS OF SPIE

SPIEDigitalLibrary.org/conference-proceedings-of-spie

# Fluorescence imaging for whole slide scanning using LED-based color sequential illumination

Leon van der Graaff, Fanny Boyaval, Lucas J. van Vliet, Sjoerd Stallinga

Leon van der Graaff, Fanny Boyaval, Lucas J. van Vliet, Sjoerd Stallinga, "Fluorescence imaging for whole slide scanning using LED-based color sequential illumination," Proc. SPIE 10679, Optics, Photonics, and Digital Technologies for Imaging Applications V, 106790D (24 May 2018); doi: 10.1117/12.2306776

SPIE.

Event: SPIE Photonics Europe, 2018, Strasbourg, France

# Fluorescence imaging for Whole Slide Scanning using LED-Based Color Sequential Illumination

Leon van der Graaff[a], Fanny Boyaval[b], Lucas J. van Vliet[a], and Sjoerd Stallinga[a]

[a]Department of Imaging Physics, Delft University of Technology, Lorentzweg 1, 2628 CJ, Delft, The Netherlands
[b]Department of Pathology, Leiden University Medical Center, Albinusdreef 2, 2333 ZA Leiden, The Netherlands

## ABSTRACT

In the field of pathology there is an ongoing transition to the use of Whole Slide Imaging (WSI) systems which scan tissue slides at intermediate resolution ($\sim$0.25 µm) and high throughput (15 mm$^2$/min) to digital image files. Most scanners currently on the market are line-sensor based push-broom scanners for three-color (RGB) brightfield imaging. Adding the ability of fluorescence imaging opens up a wide range of possibilities to the field, in particular the use of specific molecular (proteins, genes) imaging techniques. We propose an extension to fluorescence imaging for a highly efficient WSI systems based on a line scanning technique using multi-color LED epi-illumination. The use of multi-band dichroics eliminates the need for filter wheels or any other moving parts in the system, the use of color sequential illumination with LEDs enables imaging of multiple color channels with a single sensor. Our approach offers a solution to fluorescence WSI systems that is technologically robust and cost-effective. We present design details of a four-color LED based epi-illumination with a quad-band dichroic filter optimized for LEDs. We provide a thorough analysis regarding the obtained optical and spectral efficiency. The primary throughput limitation is the minimum Signal-to-Noise-Ratio (SNR) given the available optical power in the illumination étendue, and indicates that a throughput on the order of 1000 lines/sec can be obtained.

**Keywords:** Whole Slide Imaging (WSI), Digital Pathology, Fluorescence Imaging, Microscopy, Scanning, LED, epi-illumination

## 1. INTRODUCTION

Interpreting images of tissues and cells for diagnosis is a core activity of pathologists. For over a century, microscopes have been used to visualize these small structures. This has changed, however, with the emergence of digital pathology, which uses digital slide scanners to acquire high resolution ($\sim$0.25 µm) digital images of complete tissue slides ($\sim$15x15 mm) in a very short time ($\sim$1 min). These images, referred to as 'Whole Slide Images' (WSI) or 'virtual slides' are then assessed for diagnosis on a computer screen. Advantages of Digital Pathology include collaboration at a distance, correlation with radiologic images, workflow management and control, teaching, certification, and it opens the way for Computer Aided Diagnostics (CAD) and Clinical Decision Support (CDS).[1–3]

It is a major opportunity for the field of pathology for slide scanners to become compatible with fluorescence imaging. This would open the Digital Pathology environment to the benefits of both immunofluorescence studies (visualizing specific proteins) and FISH studies (Fluorescence in situ hybridization, detecting and localizing specific parts of the DNA or RNA). Both techniques offer the benefits for more reproducible and quantitative diagnosis.[4–6] Current slide scanners, however, are usually not capable of fluorescence imaging.[7] The few commercial solutions that are available, most often lack high throughput or cannot resolve multiple fluorescent dyes.

Further author information:
Sjoerd Stallinga: s.stallinga@tudelft.nl
Leon van der Graaff: l.vandergraaff@tudelft.nl

Various optical architectures for slide scanners are available,[8] for example the step-and-stitch approach which uses standard wide field acquisitions and merges them together digitally. However, the most favored architecture appears to be continuous scanning with a line sensor ('push broom' scanning), because of the mechanical simplicity and reduced need for stitching.[9] Most often, these systems make use of TDI (Time Delayed Integration) to increase the SNR.[10] Combining this design with time-sequential illumination removes the need of multiple sensors for different color channels and gives intrinsic alignment of the color channels.

Here, we propose an extension of this architecture to fluorescence scanning that is simple and robust. To achieve this, a fast switchable, high power light source is required. For that, LEDs are the most obvious choice. Advantages are a high optical power, low price, long lifetime, small size, and their availability in a wide range of colors. Usually, multi-color fluorescence imaging systems make use of mechanical filter wheels. This is, however, incompatible with line scan rates in excess of kHz rates. In our setup we have chosen to use a single 'quad-band' dichroic filter with four different reflection- and passbands and corresponding emission and excitation filters.

An intrinsic limitation to high throughput wide-field fluorescence imaging is the relative low light level that is detected, typically several orders of magnitude less than is available in brightfield imaging. This will have a big influence on the tradeoff between exposure times and the shot-noise dominated SNR, i.e. scanning will be either slow or noisy. This article will therefore focus on the efficiency of the illumination and its effect on the image quality. In the methods section, the spectral, optical and electrical efficiencies will be discussed. In our results, we describe the obtained illumination power and the resulting scanning speed that can be obtained given the required SNR.

## 2. METHODS

### 2.1 Scanning System

Our whole slide scanner prototype is based on the architecture described by Shakeri et. al.[9] (see Figure 1). We use a Nikon 20× NA 0.75 Plan Apochromat VC objective lens and a custom Nikon tube lens (effective focal length of $222.4 \pm 2.2$ mm) for obtaining a target magnification of $M = 22.24$. For lower magnification images, a Nikon 10× NA .45 Plan Apochromat $\lambda$ objective is used. A sample stage is made using two stages: a PI M-505 low profile translation stage is used for positioning of the slide in the field direction and a Newport XM1000 ultra precision linear motor stage for the continues scanning motion of the sample. To focus, we used two stages to axially translate the objective: a PI M-111 compact micro-translation stage for coarse positioning, and a PI P-721.CL0 piezo nano-positioner for fine positioning. Images are captured using a Hamamatsu Orca Flash 4.0 v2 CMOS Camera. This sensor has a pixel pitch of 6.3 µm corresponding to 0.29 µm in object space. The illumination is controlled by a National Instruments NI PXIe-6363 data acquisition card. The camera and illumination control are synchronized to the trigger output of the scanning stage.

### 2.2 Spectral efficiency

In our system we use a quad-band dichroic filter to couple in the epi-illumination. This provides us with four fixed color bands that are matched to the LED sources. This approach is compatible with color sequential illumination. In contrast to using a filter-wheel, it requires no switching time, nor synchronization and has no moving parts. Although Acousto optical tunable filters (AOTF) could provide short switching times and great spectral flexibility, they lack efficiency due their polarization sensitivity and cannot provide the suppression of excitation light needed for fluorescence applications. Using four color bands gives a good coverage of the visible spectrum and provides a good trade-off between the number of colors and spectral efficiency, as will be shown in the next paragraph.

The dichroic filter set in our setup is a Semrock BrightLine Pinkel filter set, optimized for LEDs (LED-DA/FI/TR/Cy5-4X-A-000). The used LED sources are a Ledengin LZ1 Violet LED (∼393 nm, LZ1-10UB00-00U5), and the Lumiled Luxeon Rebel Blue (∼470 nm, LXML-PB02), Lime (broad spectrum around typical wavelength 554 nm, LXML-PX02-0000) and Red (∼635 nm, LXM5-PD01) LEDs. These LEDs are manufactured as a surface mount device (SMD) and have an integrated lens of glass (Ledengin) or silicone (Lumiled) on top of the actual light emitting chip. The LEDs are soldered on metal-core printed circuit boards (MCPCB) for heat dissipation. The calculated spectral efficiencies of this configuration are shown in Figure 2. The top row

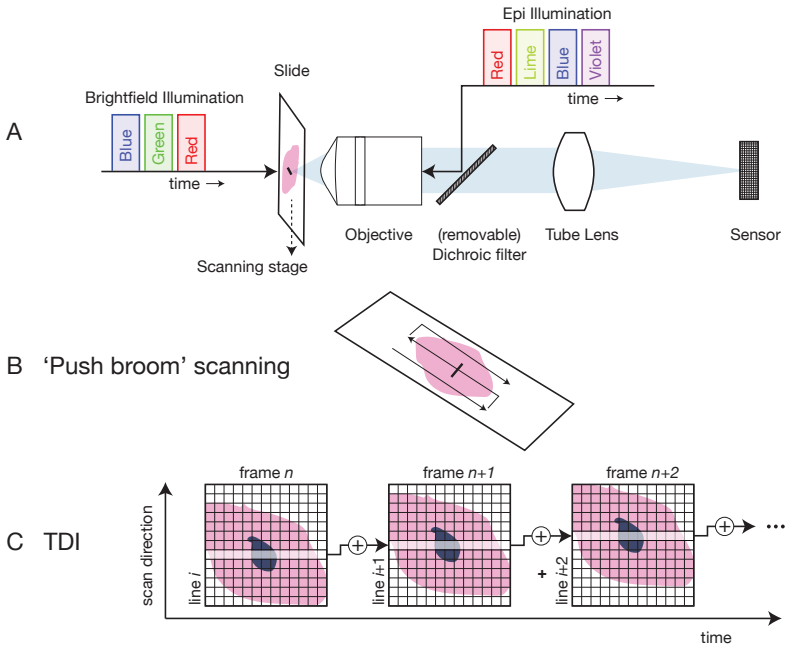


Figure 1: Illustration of the scanning system.
A. A microscope slide is translated by a scanning stage and imaged line by line on a monochromatic sensor. It is illuminated using either brightfield illumination or epi-illumination. Brightfield illumination is done sequentially with red green and blue to obtain an RGB image. For epi-illumination, the dichroic mirror is placed in the optical path and the sample is illuminated sequentially with red, lime, blue and violet to obtain multi-channel fluorescence images.
B. 'Push-broom scanning': the slide is scanned in arbitrary long lanes, back and forth over the slide.
C. Time Delayed Integration (TDI): when using a multi-line sensor, frames of sequential acquisitions can be combined to increase the signal level. For this, the movement of the slide has to be synchronized to the readout.

shows the efficiency of illumination, i.e. the product of the LED spectrum and the filter emission band, which is in general over 50 %. The lime LED has a considerable lower efficiency due to its broad spectrum. However, lime LEDs have a very high output power compared to green LEDs. This combination appears to provide more power than using an intrinsically less efficient green LED. The bottom row of Figure 2 shows the match of four commonly used fluorophores to the filter set. Again, a typical efficiency of about 50 % is expected.

### 2.3 Étendue efficiency

LEDs are available in a wide range of sizes and powers. The maximum power, however, that can be transmitted through the objective and projected onto the sample appears not to be related to the power of the light source $P_s$, but rather to its emission intensity $P_s/A_s$, where $A_s$ is the emission area of the LED. The reason for this is that in a lossless optical system, the étendue (product of area and the solid angle the source subtends) is conserved. In our case, the effectively used circular area of the LED surface $A_s = \pi R_s^2$ and the opening angle $\alpha$ used to collect the light are therefore limited by the étendue $E$ of the objective:

$$\pi R_s^2 \pi n_s^2 \sin^2 \alpha \leq E = \pi NA^2 \pi FOV^2 \tag{1}$$

where $n_s$ is the refractive index of the source material, $NA$ the numerical aperture of the objective and $FOV$ the radius of the used field of view. Two conclusions can be drawn from this inequality. First, for obtaining optimal efficiency, the LED should have a surface area $\pi R_s^2 \geq E/\pi n_s$, otherwise the étendue of the objective cannot be filled. Second, an estimate can be made of the étendue efficiency by considering the LED to be a Lambertian

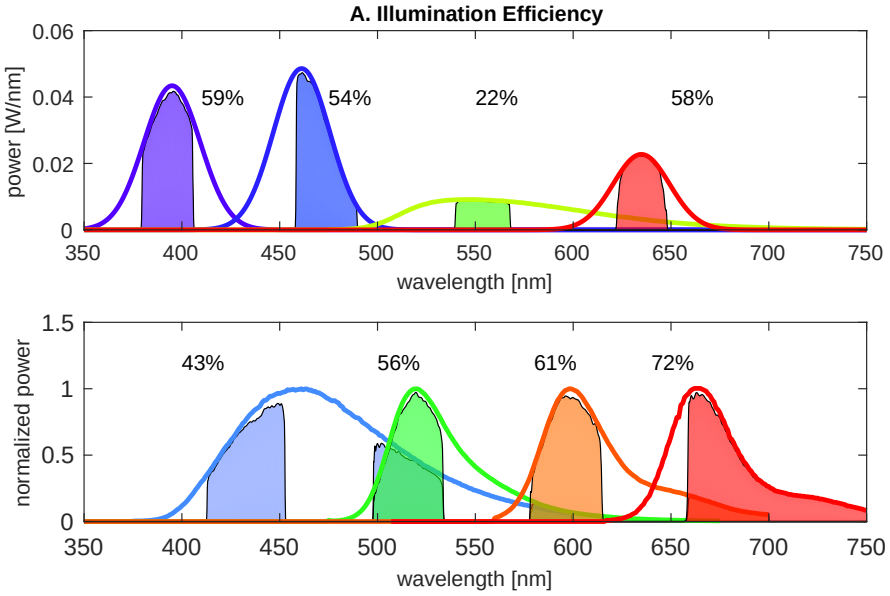


Figure 2: Spectral efficiency of the quad-band filter set.
(top) Power spectrum of the LEDs with the power spectrum after filtering indicated by the shaded area. LED and filter spectra are obtained from the data sheets provided by the manufacturers.
(bottom) Normalized power spectrum of DAPI (blue) Alexa Fluor 488 (green) Mitotracker Red (orange) and cy5 (red) with shaded the power after filtering. Fluorophore spectra are obtained from http://spectra.arizona.edu

emitter. The power that can be transmitted through the objective is then given by

$$P = \frac{P_s}{A_s}\pi R_s^2 \sin^2\alpha \leq P_s \frac{E}{A_s n_2^2 \pi} \equiv P_s \eta_E \tag{2}$$

where $\eta_E$ is the étendue efficiency and where Equation 1 is used. This shows that LEDs can be chosen arbitrary large, but only an increase of the surface intensity $P_s/A_s$ will increase the transmitted power. Filling in the relevant parameters for our system ($NA = 0.75, FOV = 0.5\,\mathrm{mm}, n_s = 1.5, A_s = 1\,\mathrm{mm}^2$) gives an estimated maximum obtainable étendue efficiency $\eta_E = 19\,\%$.

## 2.4 Optical design

The optical system is designed to have an even illumination distribution. This is achieved by using a 4f-system to image the LED sources in the back focal plane of the objective. The illumination distribution in the front focal plane (the sample plane) therefore follows the radial emission pattern of the LEDs, which is smooth and fairly uniformly distributed. An even flatter distribution profile can be obtained by having a diffuser in the back focal plane of the collector lenses at the expense of a reduction in illumination power. Therefore, a flat-field correction in post-processing is preferred. The 4f-system has a magnification of 7.5, which is made with an $f = 150\,\mathrm{mm}$ field lens (Thorlabs AC254-150-A) and $f = 20\,\mathrm{mm}$ collector lenses (Thorlabs ACL2520U-A) for the LEDs. A schematic layout of the optical design is shown in Figure 3.

## 2.5 Driver electronics

LEDs are current driven devices. In most applications, this current is either provided by the combination of a voltage source and a series resistor, or by a switched-mode power supply. Both methods are, however, not suitable for color sequential illumination, which requires short switching times (∼µs) and high thermal stability. Moreover, the LEDs are turned on only a short and limited period of time (in our case, a few ms and at most a 25 % duty cycle), which gives room for using higher currents than the maximum specified by the manufacturer. Therefore, a fast switching, high current LED driver is developed. This device makes use of optical feedback such

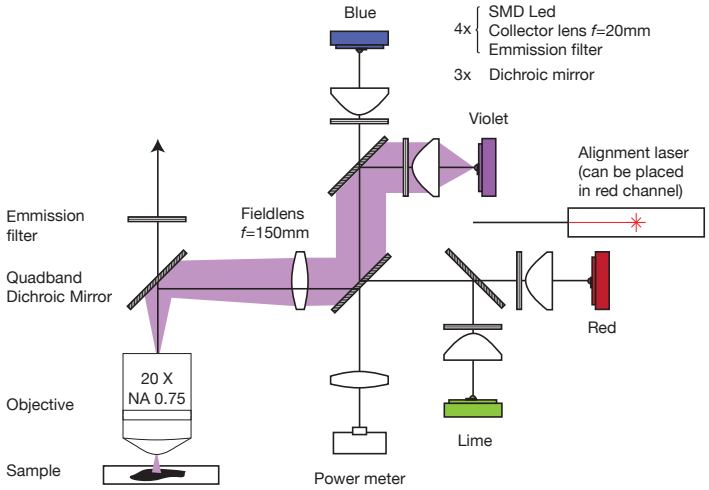


Figure 3: Schematic layout of the optical design of the LED-based epi-illumination. The optical path of the violet channel is shown shaded.

that the current can be adjusted to have a constant output power. The feedback compensates fluctuations in LED efficiency due to temperature changes. This removes the need of warming up the LEDs to a steady state temperature, and most importantly, it makes the system insensitive to all settings influencing the average current (e.g. scan speed, pulse length, number of channels) and environmental influences (e.g. room temperature, drift). The output power is measured by a Thorlabs photodetector (PDA36A) that is incorporated in the beam combiner (see Figure 3). Sharing a single detector between the color channels is possible because the LEDs are only used individually. The LED driver makes it possible to drive the LEDs with currents up to 2 A and provides switching times of at most 2 µs while it needs at most 40 µs settling time (see Figure 4-5). The speed of the driver is currently limited by the bandwidth of the photodetector.

### 2.6 Test slides

Two slides are used to demonstrate the system. The fist slide is a Thermofisher F36924 FluoCells Prepared Slide #1. This slide contains bovine pulmonary artery endothelial (BPAE) cells stained with a combination of fluorescent dyes. Mitochondria are labeled with red-fluorescent MitoTracker Red CMXRos which can be excited using the lime channel, F-actin is stained using green-fluorescent Alexa Fluor 488 phalloidin which can be excited using the blue channel, and blue-fluorescent DAPI which can be excited with the violet channel, labels the nuclei.

The second slide is an immunofluorescence staining of a stage 3 human rectum cancer. The slide is stained with three antibodies. Desmin (IgG1 M Alexa Fluor 488) is highly expressed in muscle cells and can be excited using the blue channel. CD31 (IgG R Alexa Fluor 546) is a marker for blood vessels. It is strongly expressed in endothelial cells and is therefore used to visualize the vasculature in normal and pathological conditions. This stain can be excited using the lime channel. D2-40 (direct labelled with Alexa Fluor 594) is used as a marker of lymphatic endothelium. Although this stain cannot be excited at the most optimal wavelength using our setup, it does show significant fluorescence under violet excitation. Additionally, the slide is stained with DAPI, labelling the nuclei.

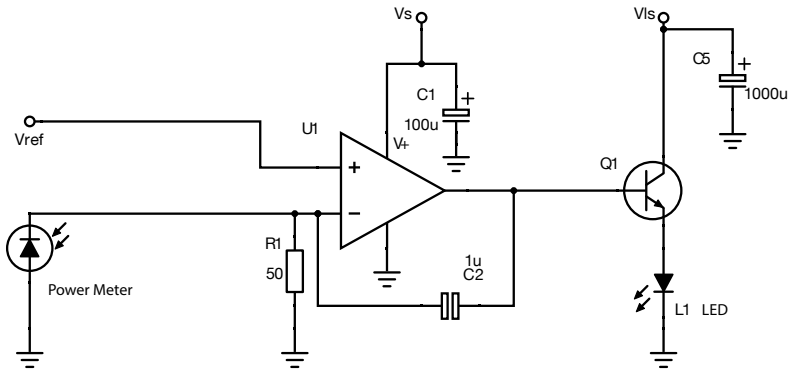


Figure 4: Schematic layout of the driver electronics. The optical feedback stabilizes the output of the LED (L1) such that the voltage measured by the power meter is equal to $V_{ref}$. The system response-time is set by R1C2, which has to be matched to the speed of the power meter in order to prevent instabilities. C1 and C5 are used for stabilization of the power supply.

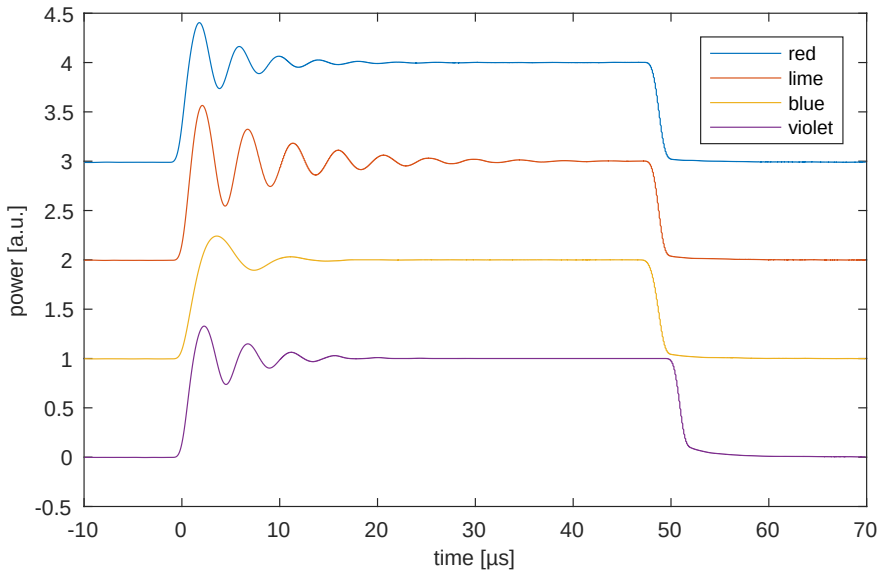


Figure 5: Switching times of the driver electronics for all four LED channels. Shown is a 50 $\mu$s pulse. The typical rise time is 2 $\mu$s. Some channels show ringing effects, which last at most 40 $\mu$s after switch-on.

## 3. RESULTS

### 3.1 Optical performance

The measured optical output of the designed epi-illumination unit is given in Table 1. The spectral efficiency is determined by measuring the LED source power both with and without the excitation filter applied. The measured efficiencies are in general somewhat higher than the expected numbers based on the theoretical spectra, listed in Figure 2. The étendue & transfer efficiency is determined by measuring the fraction of the source power that passes a circular area with a diameter of 1 mm in the front focal plane of the objective, i.e. the fraction that can actually be used for imaging. This number includes both the étendue efficiency, and the losses due to scattering and absorption. The found numbers compare reasonably well to the derived theoretical value of 19 % for a Lambertian emitter. The blue, lime and red channel loose about 50 %. The violet channel performs on par with the theoretical expectation. An explanation for the fact that the results of this channel differs significantly from the others might be found in the different LED optic. Additionally, the light of this LED might be more collimated than the assumed Lambertian emitter. The last column of Table 1 shows the optical power that can be effectively used during a 1 kHz, 25 % duty cycle pulse of 2 A peak current.

Figure 6 shows the distribution of the light in the front focal plane of the objective, which is measured by a Thorlabs CMOS camera (DCC1645C). The distribution appears rather smooth and the power remains over 70% of the peak power throughout the whole region of interest (indicated by the red circle with a diameter of 1 mm. The red channel shows some asymmetry which is caused by a slight misalignment of the LED on the PCB.

Table 1: Measured optical throughput of the illumination.

| Channel | Spectral efficiency | Étendue & Transfer efficiency | Output power [mW] |
|---|---|---|---|
| Violet | 77% | 20% | 179 |
| Blue | 78% | 9% | 73 |
| Lime | 21% | 10% | 33 |
| Red | 72% | 11% | 82 |

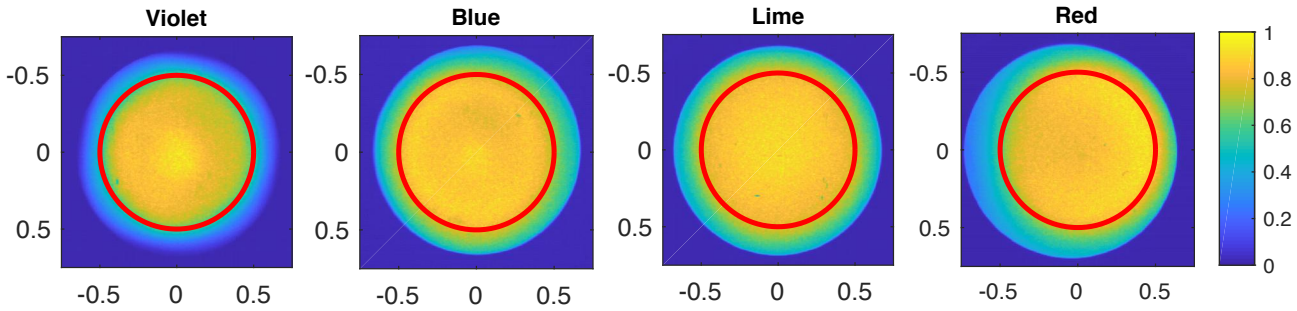


Figure 6: Measured distribution of the epi-illumination in the front focal plane of the objective. The red circle has a diameter of 1 mm and indicates the region that is actually used for imaging.

### 3.2 Scan results

Three scans are made to demonstrate the capabilities of the system. The first is a scan of the FluoCells slide, shown in Figure 7. The image shows a single-lane scan of 2048×2048 pixels (594 µm×594 µm). The scan is made using the 20× NA .75 objective lens and an exposure time of 1 ms. TDI is implemented by selecting a 96 line region of interest on the camera. The lines are aligned and summed in post-processing. There is no correction applied for background level, flat-field or crosstalk. The image shows that a high quality scan can be obtained with an exposure time of 1 ms.

The second scan is given in figure 8 (Panels A-C). The images show a whole slide scan of the human rectum tissue slide at different zoom levels. Panel A shows a whole slide scan constructed by stitching 16 scan lanes together, resulting in a 32,768×40,000 pixel image (∼19×23 mm). Panel B shows an intermediate zoom level and Panel C has the width of a single scan lane (∼1.2 mm). The scan is made using the 10× NA .45 objective lens. An exposure time of 1 ms is used while the violet channel is reduced to 17 % output power to avoid overexposure. A region of 96 lines on the sensor is used for TDI in post-processing. A correction is applied for background level and flat-field.

The third scan, given in figure 8 (Panels D-F) shows the same slide but scanned with the 20× NA .75 objective lens. Panel A shows 10 scan lanes stitched together, resulting in a 20,480×24,000 pixel image (∼6×7 mm). Panel B shows an intermediate zoom level and Panel C has the width of a single scan lane (∼0.6 mm). The same exposure time (1 ms) and illumination settings where used, but for this scan, only 16 TDI lines where used. A correction is applied for background level and flat-field.

### 3.3 Photoelectron yield

The SNR of an optical system is ultimately limited by shot noise, which has a $\sqrt{N}$ standard deviation for $N$ collected photoelectrons. It is therefore relevant to test how many photoelectrons can be captured in a practical application. To this end, a series of images is acquired of the FluoCells slide in a static alignment (i.e. without scanning) to allow repeating the experiment multiple times without alignment errors. A range of exposure times between 1 and 50 ms is used in order to vary the illumination dose. Figure 9 shows an example of the obtained images for a low dose (1 ms, Panel 9A) and a high dose (50 ms, Panel 9B). A uniform background level is present in the images, mainly due to autofluorescence. This level is determined by averaging over an area of the image where no cell structure is present, defined by selecting the 5 % pixels with the lowest intensity in the image acquired using an exposure time of 50 ms (Panel 9C). Subsequently, the background for each channel is subtracted. The representative signal is determined from averaging an area of the image with high intensities, defined by selecting the top 5 % pixels with the highest intensity in the image acquired using an exposure time of 50 ms (Panel 9D).

For every exposure time, ten noise independent images are acquired and processed. Figure 10 shows the obtained average number of collected photoelectrons per µm$^2$ (measured in object space) as a function of the exposure time. The violet channel performs very well, which can be explained by the high power of the LED and the strong fluorescence of the DAPI stain. In contrast, the number of photons obtained in the blue channel is quite low, even considering the relative power of the illumination.

The part of the human rectum slide shown in Figure 8 (Panel F) is analysed correspondingly. In this patch, the blue and lime channel have a photon yield of $1.4 \times 10^2$ and $9.0 \times 10^2$ counts/ms/µm$^2$, which is on the same order of magnitude as the yield of the FluoCells slide. The violet channel has a yield of $2.0 \times 10^4$ counts/ms/µm$^2$, where a correction is applied for the reduced excitation power. This is significantly higher than the other stains.

### 3.4 FRC Resolution

The impact of shot noise on image quality can also be assessed by its effect on the information content of the images. This is done by determining the Fourier Ring Correlation (FRC) resolution[11–13] of the images as a function of the photon count. The FRC resolution method determines the spatial frequency up to which the correlation between noise independent image acquisitions is higher than a noise threshold (typically, FRC= 1/7 is used). The inverse of this spatial frequency is the FRC resolution, and measures the smallest detail that can reliably be discerned in the image. The advantage of the FRC method is that it includes all effects of the optical imaging system, such as the noise level and the optical transfer function, but also the underlying sample structure itself. Here, we anticipate that a low SNR will lead to a smaller FRC resolution.

Ten noise independent acquisitions where done and the FRC is calculated for every independent pair. This provides an average and a standard deviation of the entire FRC curve, see for example Figure 11. The FRC resolution and the associated uncertainty can then be deduced from the threshold criterion. The obtained results are plotted in Figure 12. The measured values for the blue and lime channel are very similar: the FRC resolution improves significantly by increasing the photon counts up to $10^4$/µm$^2$, at which the Nyquist sampling distance of the sensor (580 nm) is reached. It can therefore be concluded that for photon counts below this number, the

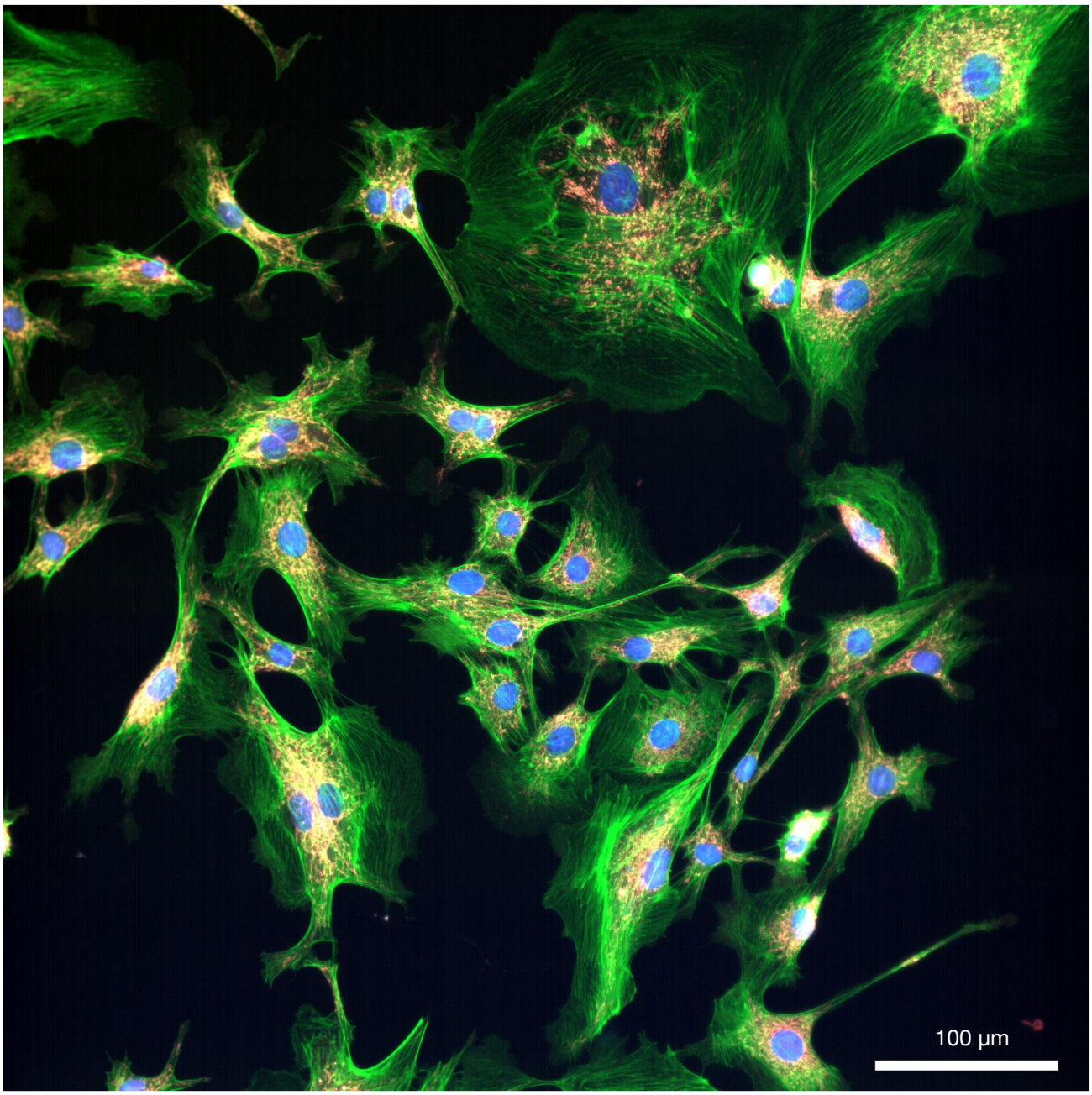


Figure 7: Scan of the FluoCells slide using 1 ms exposure time and 96 TDI lines. The displayed image is in false colors: blue corresponds to the violet excitation and labels the nuclei, green to the blue excitation and labels F-actin and red to the lime excitation and labels the mitochondria.

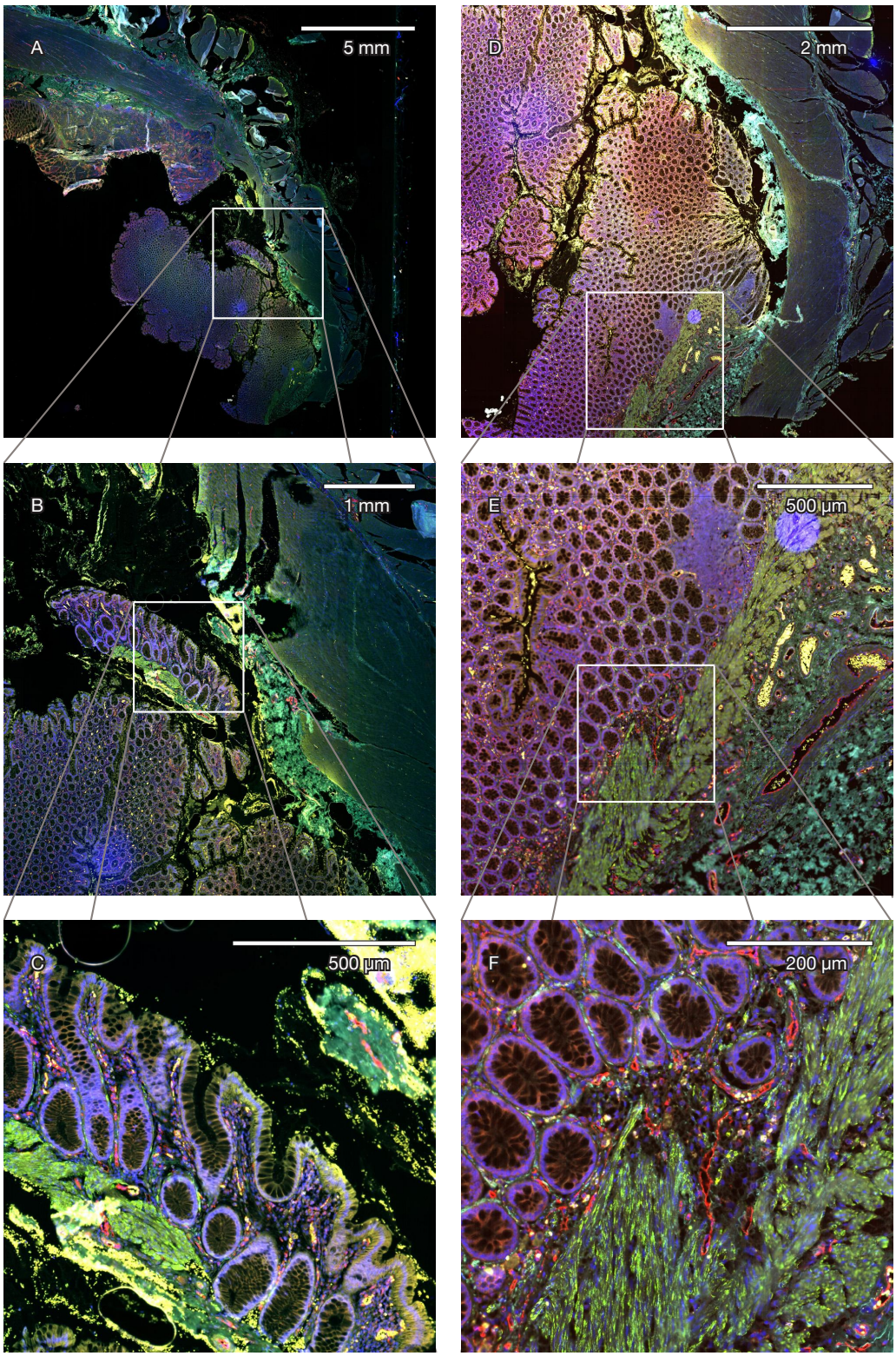


Figure 8: Scan of the human rectum slide at different zoom levels.
A-C. Acquired using the 10× NA .45 objective, an exposure time of 1 ms and 96 TDI lines.
D-F. Acquired using the 20× NA .75 objective, an exposure time of 1 ms and 16 TDI lines.

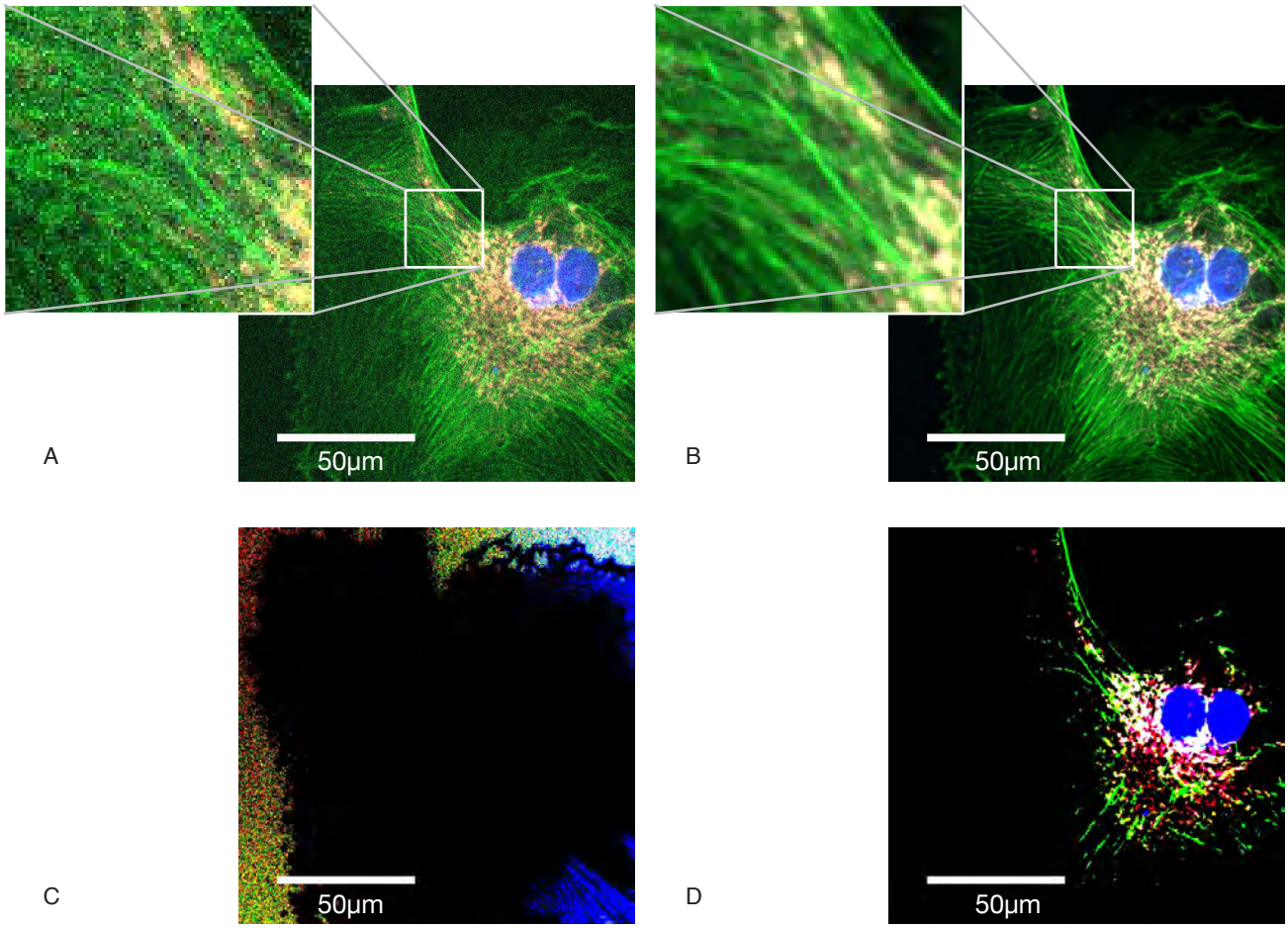


Figure 9: Thermofisher F36924 FluoCells Prepared Slide #1 in false colors. The images are made in a static alignment.
A. Image made using an exposure time of 1 ms.
B. Image made using an exposure time of 50 ms.
C. Background area, given by the 5 % pixels with lowest intensities in (B).
D. Representative area, given by the 5 % pixels with highest intensities in (B).

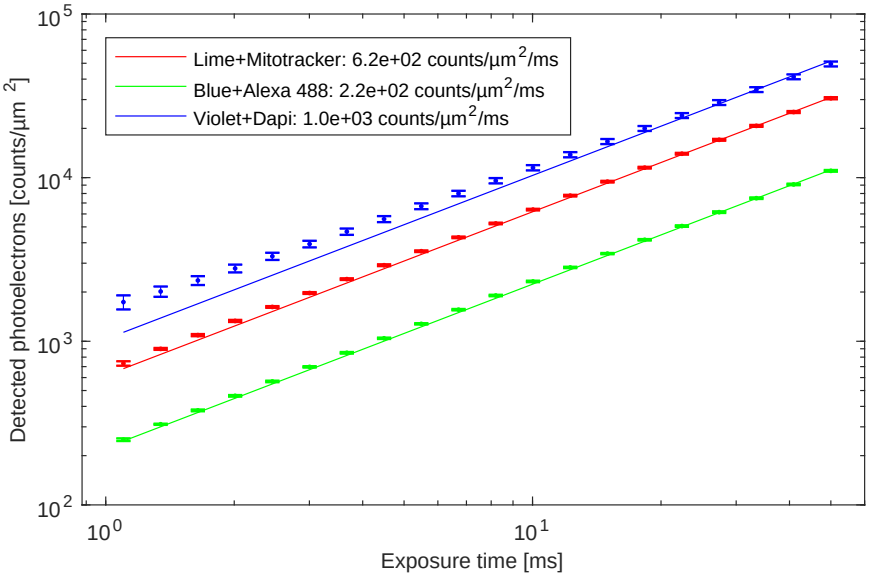


Figure 10: Photoelectron counts per µm$^2$ (measured in object space) as a function of exposure time for the 3 stains of the FluoCells slide. Error bars indicate 2 standard deviations. The straight lines indicate a linear fit with the exposure time, of which the numerical results are shown in the legend. The conversion 1 count/px = 11.7 counts/µm$^2$ is used based on the pixel pitch of 0.29 µm.

effective FRC resolution is limited by the shot-noise. Linear extrapolation to very high photon counts suggests that about $10^5$ counts/µm$^2$ have to be collected to approach the diffraction limit at $\lambda/2NA$. The violet channel shows significantly different results, which is attributed to the lack of high frequent content in the underlying sample structure compared to the blue and lime channel.

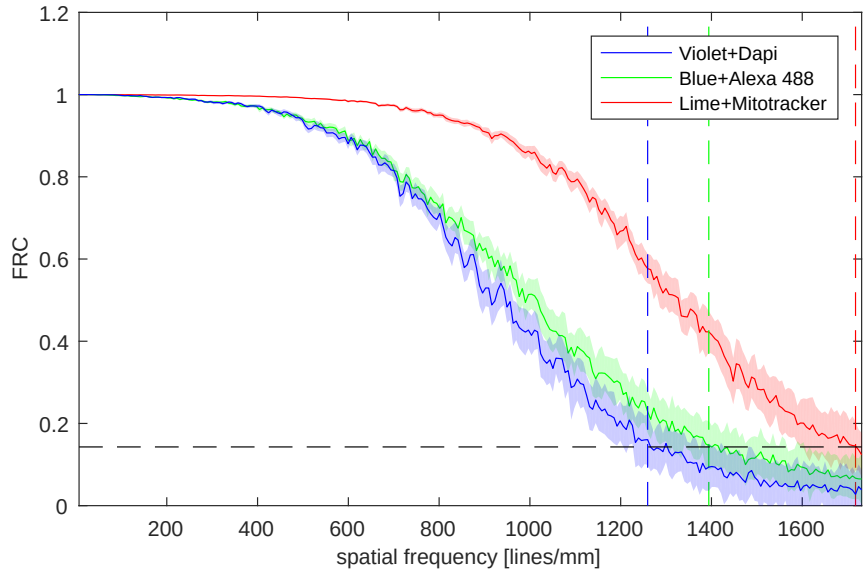


Figure 11: FRC curves of the FluoCells slide for an exposure time of 10 ms. The shaded area indicate ±2 standard deviations. The colored dashed lines indicate the FRC resolution. The black dashed line is the noise threshold of $1/7^{\text{th}}$.

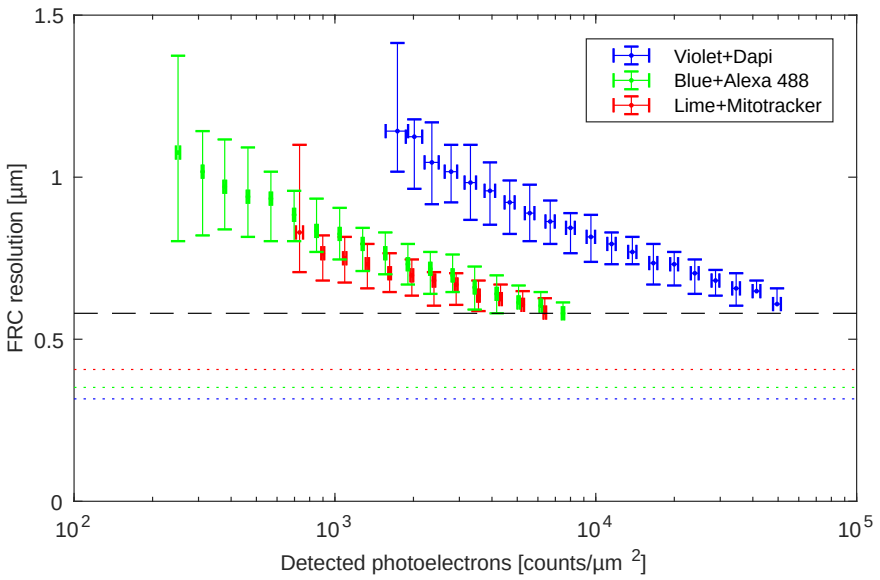


Figure 12: FRC resolution of the FluoCells slide as a function of the photoelectron counts/µm$^2$. Error bars indicate 2 standard deviations. The dotted colored lines indicate the diffraction limit for the different fluorescent labels. The dashed black line gives the Nyquist sampling limit given the pixel size and magnification of the system.

## 4. CONCLUSION & DISCUSSION

A high throughput whole slide scanning system was extended to fluorescence imaging. This was achieved by adding a LED based epi-illumination. We used multi-band dichroics and therefore no moving parts were required in the system. Our system is compatible with color sequential illumination, which enables multi color imaging using a single monochromatic sensor. The light source produces a smooth illumination pattern with rim intensities better than 70 % and has a high and stable output power. In practice, our system can capture at least 200 to 1000 photoelectrons/µm$^2$/ms. It was found that about $10^4$ photoelectrons/µm$^2$ are required to obtain an FRC resolution matching the Nyquist sampling length of the sensor (560 nm). Extrapolation of our results suggest that about an order of magnitude more photons are required to obtain true diffraction limited resolution.

Most WSI systems use continues scanning with a line sensor because of the mechanical simplicity and reduced need for stitching. The required exposure time is the main speed limitation in fluorescence imaging with LED illumination. This stands in contrast to brightfield imaging, where the throughput is limited by the digital bandwidth. Intrinsically, a step-and-stitch approach will therefore be faster than (single) line scanning for fluorescence imaging with incoherent LED illumination because it makes better use of the illumination étendue. This disadvantage of line scanning is partly overcome by the use of TDI.

Consider, for example, a three-color fluorescence image with moderate SNR. Our numbers suggest that about $10^4$ counts/µm$^2$ have be be acquired. For the dye with the lowest yield we measured (Alexa Fluor 488 in the FluoCells slide), this needs 50 ms exposure time. Using a single-line system with a field of view of 1 mm and a pixel size of 0.25 µm, scanning an area of 15 mmx15 mm in 3 colors would then take 38 h. It would require the use of 96 TDI lines to reduce the scanning time to a reasonable 23 min.

Our proposed method for extending a WSI platform to fluorescence scanning is a technologically robust and cost effective solution while adding just a few components. The obtained scanning speed is sufficient for most clinical applications where occasional scanning of fluorescent slides is needed. In this way, the benefits of fluorescence imaging can become available for the users of Digital Pathology.

## Acknowledgements

We would like to thank Noel de Miranda and Hans Morreau for their research advice.

## REFERENCES


[1] Kowal, M., Filipczuk Paweł and Obuchowicz, A., Korbicz, J., and Monczak, R., "Computer-aided diagnosis of breast cancer based on fine needle biopsy microscopic images," *Computers in biology and medicine* **43**(10), 1563–1572 (2013).

[2] Langer, L., Binenbaum, Y., Gugel, L., Amit, M., Gil, Z., and Dekel, S., "Computer-aided diagnostics in digital pathology: automated evaluation of early-phase pancreatic cancer in mice," *International journal of computer assisted radiology and surgery* **10**(7), 1043–1054 (2015).

[3] Castaneda, C., Nalley, K., Mannion, C., Bhattacharyya, P., Blake, P., Pecora, A., Goy, A., and Suh, K. S., "Clinical decision support systems for improving diagnostic accuracy and achieving precision medicine," *Journal of clinical bioinformatics* **5**(1), 4 (2015).

[4] Ghaznavi, F., Evans, A., Madabhushi, A., and Feldman, M., "Digital imaging in pathology: whole-slide imaging and beyond," *Annual Review of Pathology: Mechanisms of Disease* **8**, 331–359 (2013).

[5] Higgins, C., "Applications and challenges of digital pathology and whole slide imaging," *Biotechnic & Histochemistry* **90**(5), 341–347 (2015).

[6] Lehr, H.-A., Jacobs, T. W., Yaziji, H., Schnitt, S. J., and Gown, A. M., "Quantitative evaluation of HER-2/neu status in breast cancer by fluorescence in situ hybridization and by immunohistochemistry with image analysis," *American journal of clinical pathology* **115**(6), 814–822 (2001).

[7] Farahani, N., Parwani, A. V., and Pantanowitz, L., "Whole slide imaging in pathology: advantages, limitations, and emerging perspectives," *Pathol. Lab Med. Int* **7**, 23–33 (2015).

[8] Rojo, M. G., García, G. B., Mateos, C. P., García, J. G., and Vicente, M. C., "Critical comparison of 31 commercially available digital slide systems in pathology," *International journal of surgical pathology* **14**(4), 285–305 (2006).

[9] Shakeri, S. M., Hulsken, B., van Vliet, L. J., and Stallinga, S., "Optical quality assessment of whole slide imaging systems for digital pathology," *Optics express* **23**(2), 1319–1336 (2015).

[10] Netten, H., van Vliet, L. J., Boddeke, F. R., de Jong, P., and Young, I. T., "A fast scanner for fluorescence microscopy using a 2-D CCD and time delayed integration," *Bioimaging* **2**(4), 184–192 (1994).

[11] Nieuwenhuizen, R. P. J., Lidke, K. A., Bates, M., Puig, D. L., Grünwald, D., Stallinga, S., and Rieger, B., "Measuring image resolution in optical nanoscopy," *Nature methods* **10**(6), 557 (2013).

[12] Rosenthal, P. B. and Henderson, R., "Optimal determination of particle orientation, absolute hand, and contrast loss in single-particle electron cryomicroscopy," *Journal of molecular biology* **333**(4), 721–745 (2003).

[13] Van Heel, M., "Similarity measures between images," *Ultramicroscopy* **21**(1), 95–100 (1987).